

Adaptive Energy Dissipator with Compression-to-Tension Design

Haitao Ye, Chong Li, Shouyi Yu, Honggeng Li, Yiling Lian, Xiangnan He, Juzheng Chen, Xingjian Huang, Liuchao Jin, Jianxiang Cheng, Rong Wang, Lixi Huang, Biao Zhang, Xu Song, Yang Lu,* and Qi Ge*

Energy-dissipating materials are vital for daily life and engineering applications. Among all the energy-dissipating materials, the polymer-based ones are reusable and loading rate-dependent, but suffer from two limitations: i) they cannot synchronously achieve high loss factor and high modulus; ii) their stretch-induced high energy dissipation capability cannot be fully used in compression-dominated applications. To address them, a high-energy-dissipating (HED) polymer is reported with two types of dynamic physical crosslinks (hydrogen bonds and dynamic coordination bonds) to obtain a high loss factor ($\tan\delta$ up to 2), modulus (110.5 MPa), and dissipated energy density (26.8 J cm⁻³). To fully liberate its stretch-dominated dissipation under compression, HED-based compression-to-tension (C2T) structures are designed that convert compression into tension on the HED strips. Multimaterial 3D printing is utilized to fabricate such C2T structures whose energy dissipation capability is tunable and \approx 100 times higher than that of HED-based octet lattices. Furthermore, the C2T structures are used to develop artificial intervertebral discs and low-frequency vibration isolators to demonstrate their adaptive capability of dissipating impact and vibration energies in bio-implants and precision instruments. The proposed HED polymers and their C2T structures offer a new way to design and develop high-performance energy-dissipating metadevices.

1. Introduction

Energy-dissipating materials are widely used in daily life and engineering applications for impact protection^[1,2] and vibration isolation.^[3,4] Traditional energy-dissipating materials include metals,^[5,6] foams,^[7,8] fiber-reinforced composites,^[9,10] and others,^[11,12] which dissipate mechanical energy mainly through inelastic mechanisms (e.g., plastic deformation, fracture, or fragmentation).^[13–15] However, they can only be used once, since the materials are permanently damaged during the energy dissipation process. Recently, researchers have reported architected materials that trap energy through elastic buckling.^[16–18] Although these structures are reusable, their energy dissipation capability is fixed and independent of loading rates due to the elastic buckling mechanisms. Thus, the development of materials that are both reusable and exhibit rate-dependent enhancement in energy dissipation remains a significant challenge.

H. Ye, S. Yu, X. He, X. Huang, L. Jin, J. Cheng, R. Wang, Q. Ge
 Shenzhen Key Laboratory for Additive Manufacturing of
 High-Performance Materials
 Department of Mechanical and Energy Engineering
 Southern University of Science and Technology
 Shenzhen 518055, China
 E-mail: geq@sustech.edu.cn

H. Ye, J. Chen
 Department of Mechanical Engineering
 City University of Hong Kong
 Kowloon, Hong Kong SAR, China

C. Li, Y. Lian, L. Huang, Y. Lu
 Department of Mechanical Engineering
 The University of Hong Kong
 Pokfulam Road, Hong Kong SAR, China
 E-mail: [yru1@hku.hk](mailto:ylu1@hku.hk)

H. Ye, L. Jin, X. Song
 Department of Mechanical and Automation Engineering
 The Chinese University of Hong Kong
 Hong Kong SAR 999077, China

H. Li
 School of Engineering
 Great Bay University
 Dongguan 523000, China

B. Zhang
 Xi'an Institute of Flexible Electronics
 Northwestern Polytechnical University
 127 West Youyi Road, Xi'an 710072, China

Y. Lu
 Materials Innovation Institute for Life Sciences and Energy (MILES)
 HKU-SIRI, Shenzhen 518000, China

 The ORCID identification number(s) for the author(s) of this article can be found under <https://doi.org/10.1002/adfm.202521393>

DOI: 10.1002/adfm.202521393

A promising pathway toward this goal involves polymer-based systems, which are inherently viscoelastic and rate-sensitive. In recent years, various such materials have been developed, including amorphous polymers with viscoelasticity,^[19,20] polymer-fluid gels (PFG) with viscous polymer fluid infused in elastic networks,^[21–23] shear-thickening fluids (STF) relying on weak dynamic crosslinks,^[24–26] and liquid crystal elastomers (LCE) with reconfigurable mesogen domains.^[14,27–29] Although these energy-dissipating materials are reusable and loading rate-dependent, they still face two limitations. i) They cannot synchronously achieve a high loss factor ($\tan\delta > 1$) and high modulus (>20 MPa) (Table S1, Supporting Information). For instance, the previously reported PFG and STF have high loss factors ($\tan\delta > 1$) but low modulus (below 20 MPa),^[19,20,22,24,26] making them incompetent to dissipate high impact energy. ii) High stretchability of the above materials makes them capable of dissipating much more energy under tension than under compression. However, in most practical applications, the energy-dissipating materials are under compression, which suppresses the tension-induced high energy dissipation capability of these materials.

To overcome these limitations, researchers have begun to explore the use of 3D printing to structuralize these polymer-based materials,^[28,30,31] creating architected metamaterials (i.e., lattice and auxetic metamaterials^[32,33]) that leverage geometric design to achieve superior performance. Among various architected types, stretch-dominated structures^[34,35] are particularly promising, as they dissipate energy primarily through the efficient axial tension or compression of their members, leading to high specific energy absorption. In contrast, bending-dominated structures^[34,36] rely on a less efficient bending mechanism at the nodes or ligaments, which often results in stress concentration and underutilization of the material's intrinsic strength.^[31] However, most existing stretch-dominated structures are fabricated from single materials, which inherently cannot combine high modulus with large deformability. Consequently, these structures still undergo inefficient global buckling or strut bending beyond certain strain levels, limiting their energy dissipation. Recently, several attempts have employed multimaterial 3D printing to create systems such as compression-to-tension transformed origami structures,^[11,37] which combine rigid materials with elastomers. By converting global compressive loads into localized tensile deformation of the elastomers, these designs achieve repeatable load-bearing. Nonetheless, the energy absorption capacity of such configurations remains limited by the intrinsically low energy dissipation and finite deformation range of the elastomeric components.

Here, we develop high-energy-dissipating (HED) polymers that have a high loss factor ($\tan\delta$ up to 2.0), high modulus (up to 110.5 MPa), high stretchability (up to 1470.7%), as well as high dissipated energy density (up to 26.8 J cm^{-3}). We attribute such extraordinary energy dissipation capability of the HED polymer to two types of dynamic physical crosslinks resulting from hydrogen bonds and dynamic coordination bonds, which are validated experimentally and theoretically. To fully liberate tension resulting in high energy dissipation of the HED polymers, we design HED-based compression-to-tension (C2T) structures, which convert compression on them to tension on the HED strips. We utilize digital light processing (DLP)-based multimaterial 3D printing to fabricate such C2T structures whose energy dissipation capability is adaptive by tuning the geometric parameters, and

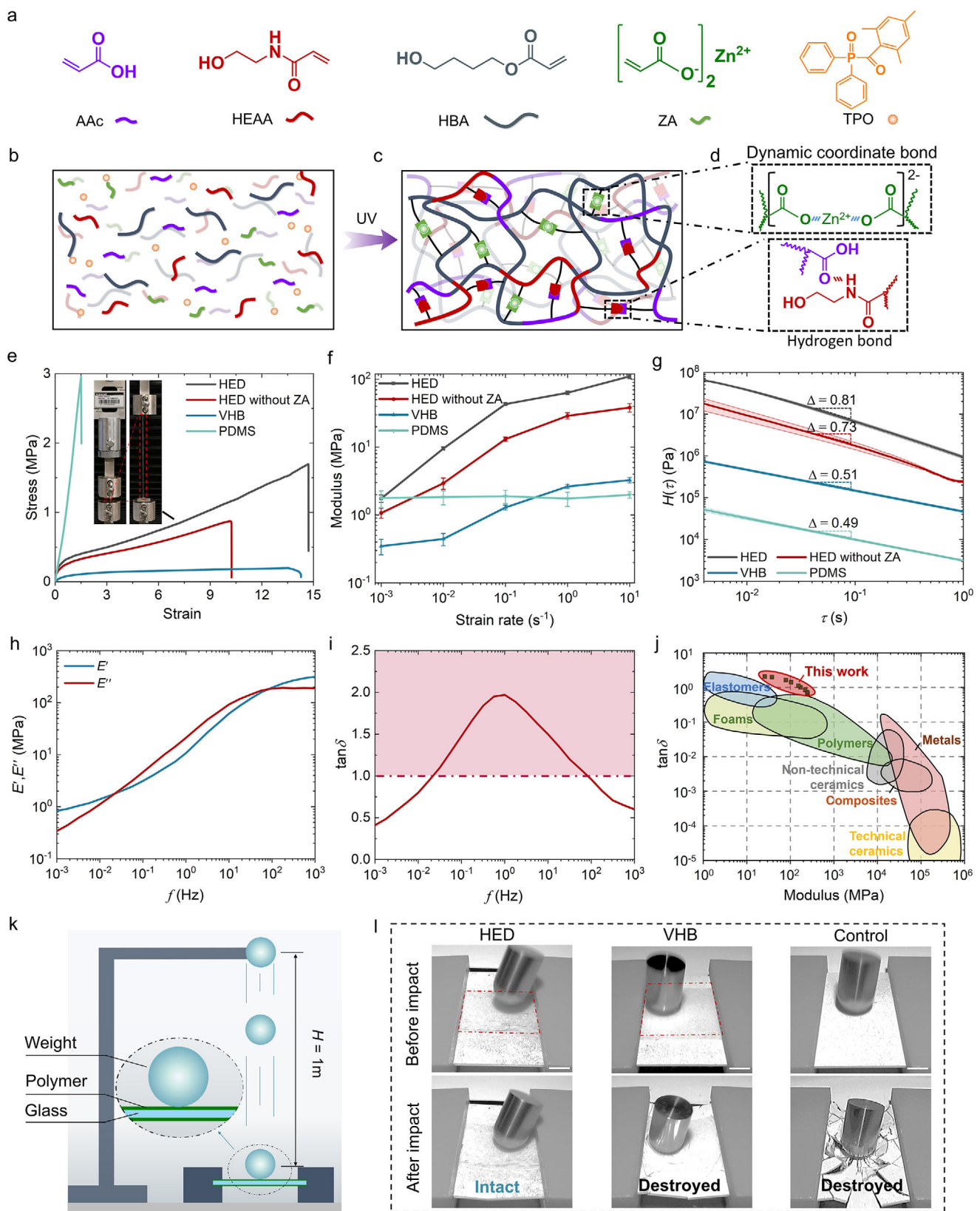
is ≈ 100 times higher than that of octet structures made of pure HED polymer. Furthermore, we use the C2T structures to form artificial intervertebral discs and low-frequency vibration isolators to demonstrate their adaptive capability of dissipating impact and vibration energies. Therefore, the proposed HED polymers and their C2T structures pave an efficient way to design and fabricate energy-dissipating metadevices with high energy-dissipation capability and adaptivity for various applications, including electronics, bio-implants, precision instruments, and others.

2. Results and Discussion

2.1. Chemicals and Characterizations for HED Polymers

Figure 1a presents the chemicals used to prepare the HED polymer precursor solution that consists of four mono-acrylate monomers: 12.5 wt.% acrylic acid (AAc), 12.5 wt.% N-(2-Hydroxyethyl) acrylamide (HEAA), 75 wt.% 4-hydroxybutylacrylate (HBA), as well as 0.75 wt.% zinc acrylate (ZA) of the total weight of monomers. In addition, we add 2 wt.% 2,4,6-trimethylbenzoyl diphenylphosphine oxide (TPO) of the total weight of monomers as a photoinitiator. Details for the chemicals can be found in the Experimental Section. As illustrated in Figure 1b–d, UV irradiation triggers photopolymerization that converts liquid precursor solution (Figure 1b) into solid material (Figure 1c) where the high-molecular-weight linear chains with a wide range distribution ($M_w = 42\,179 \text{ g mol}^{-1}$, PDI = 2.503 in Figure S1, Supporting Information) and are physically crosslinked by two types of dynamic physical bonds (illustrated in Figure 1d and experimentally confirmed in Figure S2, Supporting Information): i) hydrogen bonds between the hydrogen atoms from amine or hydroxyl groups and the oxygen atoms from carboxyl groups; ii) dynamic coordination bonds between zinc ions and the oxygen atoms from carboxyl groups. The presence of these bonds was experimentally confirmed by Fourier transform infrared (FTIR) spectroscopy (Figure S2, Supporting Information). Specifically, the broad O–H stretching band at 3345 cm^{-1} indicated hydrogen bonding, while the downshift of the asymmetric $-(\text{COO})-$ vibration to lower wavenumbers in the HED polymer confirmed coordination between carboxylate groups and Zn^{2+} ions. This unique network structure endows the HED polymer with exceptional mechanical properties such as high stretchability, high strain-rate dependent mechanical response, and high loss factor, even in humid environments (Figure S3, Supporting Information).

Figure 1e shows the quasi-static extension tests that compare the stress-strain behaviors between the commercial elastomers with chemical crosslinks (i.e., PDMS and VHB, details can be seen in the Experimental Section) and the HED polymers with dynamic physical bonds. For the commercial elastomers, Young's modulus and stretchability become contradictory properties as the increase in crosslinking density leads to the rise in Young's modulus, but inevitably sacrifices the stretchability. In contrast, the HED polymers can be stretched by ≈ 15 times and also have a moderate modulus (8.6 MPa). Detailed Young's modulus and stretchability of the tested materials are summarized in Table S2 (Supporting Information). We attribute this superior mechanical property of the HED polymers to the long linear chains formed by the mono-acrylate functional groups and the existence of



dynamic physical bonds. It should be noted that compared with the HED polymer only having hydrogen bonds (HED without ZA in Figure 1e), the introduction of dynamic coordinate bonds (adding only 0.75 wt.% zinc acrylate) significantly enhances the HED polymer in both stretchability (from 1022.5% to 1470.7%) and Young's modulus (2.9 to 8.6 MPa).

Moreover, as shown in Figure 1f and Figure S4 (Supporting Information), the stress-strain behavior of the HED polymers exhibits extremely high strain-rate dependence. The Young's modulus of a HED polymer escalates by 63 times from 1.75 to 110.5 MPa (for HED without ZA: from 1.1 to 38.3 MPa), when the strain rate increases from 0.001 to 10 s⁻¹. In contrast, under the same variation range of strain rates, the modulus of the commercial elastomers increases slightly (PDMS: from 1.78 to 1.98 MPa; VHB: from 0.35 to 3.3 MPa). Details on Young's modulus variations under different strain rates can be found in Table S3 (Supporting Information). This extreme rate-sensitivity is characteristic of a broad relaxation spectrum, arising from the wide molecular weight distribution and, more critically, the dynamic physical bonds. Under high strain rates, these bonds act as locked crosslinks, raising the modulus, while at low rates, their dissociation and reorganization enable energy dissipation and flow. To validate this hypothesis, we conducted frequency sweep tests on the above materials to establish the relation between storage/loss modulus (storage modulus: E' , loss modulus: E'') and sweep frequency f (0.1–50 Hz). Details on the frequency sweep tests are provided in Materials and Methods. The frequency-dependent storage/loss modulus can be described by the Maxwell model (Text S5 and Figure S5, Supporting Information):

$$\begin{aligned} E' &= \int_{-\infty}^{\infty} H(\tau) \frac{\omega^2 \tau^2}{1 + \omega^2 \tau^2} d(\ln \tau), E'' \\ &= \int_{-\infty}^{\infty} H(\tau) \frac{\omega \tau}{1 + \omega^2 \tau^2} d(\ln \tau) \end{aligned} \quad (1)$$

where $H(\tau)$ is the relaxation time spectrum at relaxation time τ , and ω is angular frequency ($\omega = 2\pi f$). By using Equation (1) to fit the $E'-f$ curves in Figure S6 (Supporting Information), we obtain the relaxation time spectrum-relaxation time curves (Figure 1g) for the HED polymers, VHB, and PDMS, respectively. In Figure 1g, for all four materials, the relaxation time spectrum $H(\tau)$ drastically drops as the relaxation time τ extends. However, compared with other materials, the HED polymer has a higher $H(\tau)$ that decreases from 64 to 0.95 MPa with a steeper logarithmic slope ($\Delta = \log H / \log \tau$). The higher $H(\tau)$ of the HED polymer might result from its higher modular weight and more dynamic physical bonds (compared with HED without ZA) that form more physical crosslinks.^[38,39] The wider molecular weight distribution of the HED polymer (Figure S1, Supporting Information) leads

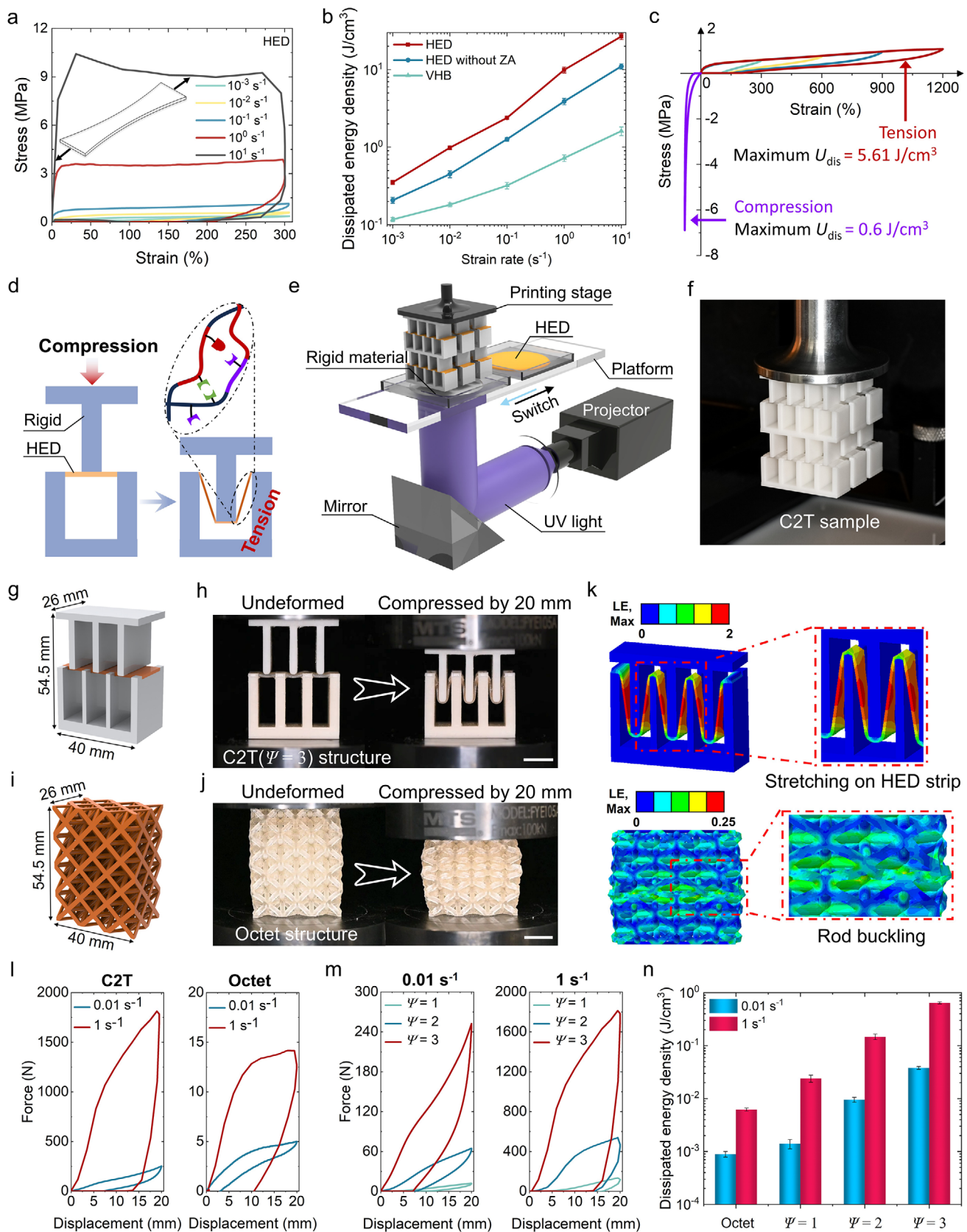
to a steeper Δ so that the modulus of the HED polymer varies drastically over a wider strain-rate range.^[40]

Besides the highly strain-rate dependent mechanical response, the HED polymer also exhibits excellent capability of energy dissipation. As shown in Figure 1h, we employ the time-temperature superposition principle (Text S6, Supporting Information) to investigate the variations of E' and E'' of the HED polymer over a wider range of frequency (0.001–1000 Hz). Remarkably, in the frequency range from 0.02 to 83 Hz, the loss modulus E'' is even higher than the storage modulus E' , which leads to a high loss factor ($\tan \delta = E''/E'$) over the whole frequency range (Figure 1i). Remarkably, $\tan \delta$ is greater than 1 (up to 2) when f is from 0.02 to 83 Hz; even at a wider frequency range (from 0.002 to 1000 Hz), $\tan \delta$ is always >0.5 . The high loss factor makes the HED polymer become an ideal material for energy dissipation. Figure 1j presents $\tan \delta$ -modulus relations for the previously reported energy-dissipating materials. Details can be seen in Table S4 (Supporting Information). In general, high loss factor and high modulus are conflicting properties. For example, elastomers have high $\tan \delta$ (>1) but low modulus (<5 MPa), while metals or metallic structures have high modulus (>1 GPa) but low $\tan \delta$ (<0.1).^[41,42] The high strain-rate-dependent modulus and high loss factor allow the HED polymer to manage the two conflicting properties, making it have a higher modulus while maintaining high $\tan \delta$ compared with traditional energy-dissipating elastomers. To further demonstrate the excellent energy dissipation capability of the HED polymer, we conducted drop weight impact tests. As illustrated in Figure 1k, a 300 g weight drops from 1 m above the glass plate, which is coated with white color and covered with the HED polymer thin films (thickness: 1 mm). In Figure 1l and Movie S1 (Supporting Information), the glass plate protected by the HED polymer remained intact after impact. In contrast, the glass plate without film (control) was smashed into pieces, and the glass plate covered with the VHB film was broken by the impact.

2.2. Compressive Energy-Dissipating Structure via Compression-to-Tension Design

The exceptional mechanical properties (high stretchability, high strain-rate-dependent modulus, and high loss factor) allow the HED polymer to dissipate a large amount of energy when it is under a tensile loading-unloading cycle. Figures 2a and S7 (Supporting Information) present tensile loading-unloading cycles of the HED, HED without ZA, and VHB polymers under different strain rates (from 10⁻³ to 10 s⁻¹). Details on the experiments can be seen in Materials and Methods. As shown in Figure 2a, as both Young's modulus and strength of the HED polymer are highly strain-rate dependent (Table S3, Supporting Information), the hysteresis loop drastically expands when the strain rate

Figure 1. Chemicals and Characterizations of HED Polymers. a) Chemicals used to prepare the HED polymer precursor. b–d), Photopolymerization process that converts the liquid precursor solution of HED polymer (b) into a solid polymer network (c), which has two types of physical crosslinks (d). e) Comparison of the quasi-static tensile stress-strain curves between HED polymers and commercial elastomers. f) Comparison of the strain-rate-dependent Young's modulus between HED polymers and commercial elastomers. g) Comparison of the relaxation time spectrum ($H(\tau)$) between HED polymers and commercial elastomers. h) Variation of storage modulus (E') and loss modulus (E'') over loading frequency from 0.001 to 1000 Hz. i) Loss factor ($\tan \delta$) over loading frequency from 0.001 to 1000 Hz. j) Performance chart comparing the $\tan \delta$ -modulus relation between the HED polymer and previously reported energy-dissipating materials. k) Schematic illustration of drop-weight impact test. l) High-speed snapshots of the glass plates before and after impact. Scale bar: 10 mm.



increases. Figure 2b plots the variations of dissipated energy density (U_{dis}) of the three polymers under different strain rates. Here, the dissipated energy density can be calculated as $U_{\text{dis}} = U - U_{\text{ela}}$, where U and U_{ela} are the total input strain energy density and the released elastic energy density (Text S8 and Figure S8, Supporting Information). For the HED polymer, the dissipated energy density escalates significantly when the strain rate increases (detailed data can be found in Table S5, Supporting Information), and remarkably reaches 26.8 J cm^{-3} when the strain rate reaches 10 s^{-1} , which is higher than that of HED without ZA (11.0 J cm^{-3}) and VHB (1.6 J cm^{-3}). The energy dissipation capability of the HED polymer is much higher than that of previously reported PFG (0.1 J cm^{-3}),^[19] LCE (0.55 J cm^{-3}),^[28] and STF (1.8 J cm^{-3}).^[26] Moreover, the dissipated energy density of the HED polymer is highly dependent on the applied maximum strain (ε_{max}). As shown in Figure 2c, when the HED polymer is stretched under a strain rate of 0.1 s^{-1} , the dissipated energy density elevates from 0.88 to 5.61 J cm^{-3} as ε_{max} increases from 300% to 1200% (Figure S9a, Supporting Information), indicating that more energy can be dissipated when the HED polymer is stretched more. In contrast, the energy dissipation capability is significantly suppressed under compression as it only reaches 0.60 J cm^{-3} when the HED polymer is compressed by 80% (Figure S9b, Supporting Information). From Figure 2c, we conclude that the HED polymer exhibits unsymmetric energy dissipation capability under tension and compression. Due to the high stretchability, the maximum dissipated energy under tension can be about ten times that under compression.

However, in the majority of practical applications, energy-dissipating materials are subjected to compression to dissipate adverse mechanical energies resulting from impact, vibration or other sources.^[20,27,43] To fully liberate the tension-resulted high energy dissipation of the HED polymer for practical applications, we design a compression-to-tension (C2T) structure (Figure 2d) which comprises three components: two rigid polymer frames ("T" shape top frame and "U" shape bottom frame) and a HED polymer strip. When under compression, the top "T" frame is pushed downward resulting in a large stretch on the HED polymer strip and converting vertical compression (push) to tension (pull) on the HED polymer strip. Moreover, since the HED polymer is highly photocurable with low viscosity (Figure S10, Supporting Information), we can use a commercial multimaterial DLP 3D printer (Figure 2e) to fabricate the C2T structure (Figure 2f), and show good adhesion between the HED polymer and the rigid polymer after multiple cycles of loading (Figure S11, Supporting Information).

tion). Details on 3D printing can be found in Materials and Methods.

To investigate its capability of energy dissipation, as shown in Figure 2g, we design a C2T structure with three sections ($\Psi = 3$), and then compress the printed artifact by a displacement of 20 mm (Figure 2h). For comparison, we also design an octet truss structure (Figure 2i), which has the same volume and relative density as that of the C2T structure. We print the octet truss structure by using the HED polymer, and compress it by 20 mm (Figure 2j). Comparing Figure 2h,j, it is obvious that the HED polymer strip in the C2T structure is highly stretched while the rods in the octet truss are buckled. We performed the finite element (FE) simulations to visualize the local deformation on the C2T and octet truss structures. As shown in Figure 2k, the maximum local tensile strain on the C2T structure reaches 160% . In contrast, the maximum strain on the buckled rods of the octet truss is $<20\%$. Details on the FE simulation model are introduced in Text S12 and Figures S12 and S13 (Supporting Information). We further conducted compressive experiments to compare the mechanical responses between the C2T and octet truss structures. Details on the experiments can be seen in Experimental Section. Figure 2l presents the loading-rate dependent force-displacement relations between the C2T and octet truss structures. Under loading rate of $54.5 \text{ mm}\cdot\text{s}^{-1}$ (strain rate: 1 s^{-1}), the maximum force on the C2T structure reaches 1811.7 N , and dissipated energy is 19.0 J . In comparison, under the same loading rate, both maximum force and dissipated energy of the octet truss structure is ≈ 100 times lower. Similarly, the Kelvin truss structure exhibits even more reduced performance, with its maximum force and dissipated energy being ≈ 180 times lower than those of the C2T design (Figure S14, Supporting Information). This significant enhancement is primarily attributed to the compression-to-tension design, which fully exploits the tensile properties of the HED polymer. Detailed comparison can be seen in Table S7 (Supporting Information). More importantly, the high printability of the HED polymers allows high designability. As shown in Figure S15 (Supporting Information), we design and print the C2T structures with different numbers of sections ($\Psi = 1, 2, 3$). Figure 2m,n shows that the C2T structure with more sections dissipates more energy due to higher strains on the HED polymer strips (Figure S16, Supporting Information).

2.3. 3D C2T Structure with Adaptive Energy Dissipation for Potential Application as Artificial Intervertebral Disc

Intervertebral disc (IVD), as illustrated in Figure 3a, is a cartilage tissue that maintains spinal flexibility and provides shock

Figure 2. Compression-to-tension design for enhanced energy dissipation under compression. a) Stress-strain behavior of HED polymer stretched by up to 300% at different strain rates. b) Dissipated energy density of VHB, HED without ZA, and HED polymers at varied strain rates. c) Energy dissipation comparison of HED polymer under compression and tension (Strain rate = 0.01 s^{-1}). d) Mechanism of C2T structure converting compressive load to tensile deformation on HED strip. e) Fabrication of C2T structure through multi-material DLP 3D printing approach. f) Snapshot of printed C2T structure. g–j) Compressive tests on the C2T structure and octet truss structure with the same volume and relative density: geometric models are illustrated in (g) and (i), and compressive processes are shown in (h) and (j). k) FE simulations comparing the local deformations on the C2T and octet truss structures. l) Compressive force-displacement responses of C2T and octet truss structures at strain rates of 0.01 s^{-1} (loading speed: 0.545 mm s^{-1}) and 1 s^{-1} (loading speed: 54.5 mm s^{-1}). m) Rate-dependent compression performance of C2T structures with varying section numbers ($\Psi = 1–3$). n) Comparison of dissipated energy density between octet truss structure and C2T structures with different sections ($\Psi = 1, 2, 3$) under strain rates of 0.01 and 1 s^{-1} (loading speed: 54.5 mm s^{-1}). Scale bar: 10 mm .

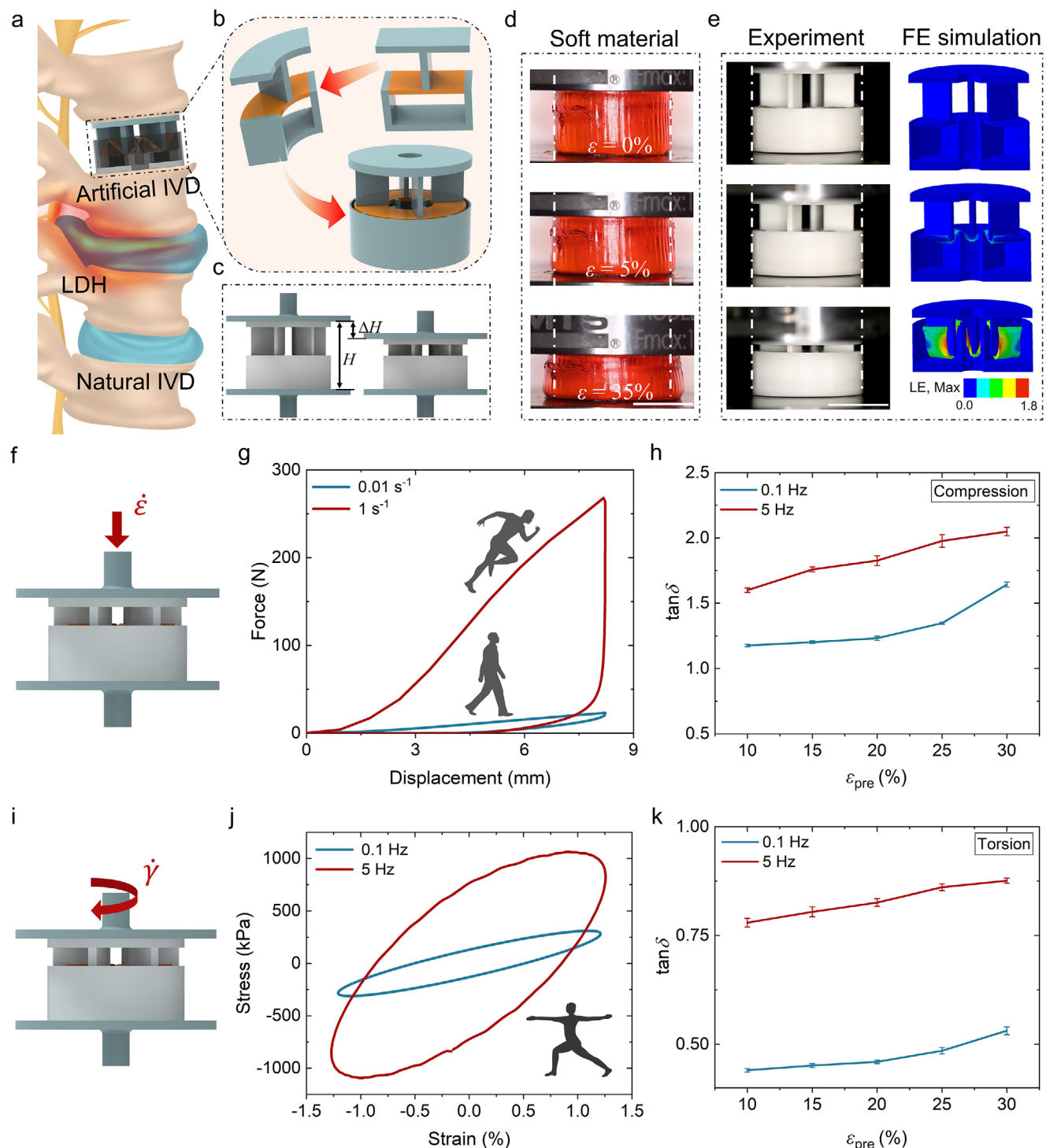


Figure 3. Design and characterization of an artificial IVD constructed by C2T structures. a) Spinal anatomy schematic showing artificial IVD, natural IVD, and LDH. b) Design evolution of a C2T artificial IVD. c) Schematic illustration presenting the compressive pre-strain (ε_{pre}) on the C2T artificial IVD. d) Compression on an artificial IVD made of pure soft material. e) Compression on a C2T artificial IVD and the FE simulation. f) Schematic illustration of compression on the C2T artificial IVD under different strain rates ($\dot{\varepsilon}$). g) Loading-unloading tests on the C2T artificial IVD at loading strain rates of 0.01 s^{-1} and 1 s^{-1} . h) Variation of loss factor ($\tan \delta$) achieved from the compressive loading-unloading tests under different compressive pre-strains and loading frequencies. i) Schematic illustration of the cyclic torsion tests on the C2T artificial IVD under different shear strain rates ($\dot{\gamma}$). j) Lissajous curves achieved from the cyclic torsion tests at torsional frequencies of 0.1 and 5 Hz. k) Variation of loss factor ($\tan \delta$) achieved from the cyclic torsion tests under different compressive pre-strains and loading frequencies. Scale bar: 15 mm.

absorption.^[44] Long-term compression and torsion may lead to lumbar disc herniation (LDH), which leads to severe pain, mobility issues, or even disability caused by nucleus pulposus bulging and subsequent spinal cord compression.^[45,46] Traditional treatments, such as surgical removal or spinal ablation, often have high recurrence rates or limit spinal motion.^[47] As a result, IVD replacement has become a main surgical alternative. However, most artificial IVDs are metal-based structures and have higher stiffness than natural IVDs, which may cause chronic pain resulting from stress shielding.^[45] Recently developed polymer-based artificial IVDs^[48,49] match the stiffness of natural IVDs, whereas the low stiffness of polymers makes them incapable of dissipating the high energy generated by dynamic body movements.

Here, we design an artificial IVD by rotating the 2D HED polymer-based C2T structure (Figure 3b). To mimic the static load resulting from body weight, a compressive pre-strain (ε_{pre} , $\varepsilon_{\text{pre}} = \Delta H/H$) is initially applied to the artificial IVD (Figure 3c). Unlike the artificial IVD made of pure soft material, which expands laterally under compression due to Poisson's ratio effect (Figure 3d), the C2T structure-based artificial IVD maintains zero lateral expansion under compression (Figure 3e) to avoid compression to the spinal cord. FE simulations reveal that the compression applied to the structure is converted to large tension on the HED polymer strips.

More importantly, this C2T structure design endows the artificial IVD with excellent capability of dissipating mechanical energies from daily body motions. As illustrated in Figure 3f, we conducted compression tests under different strain rates (0.01 s^{-1} and 1 s^{-1}) to evaluate the energy dissipation capability of the artificial IVD under walking and running scenarios, which is reflected by the loading-unloading curves presented in Figure 3g. When the loading strain rate increases from 0.01 and 1 s^{-1} , the stiffness of the artificial IVD escalates by 14.7 times from 3.1 to 45.5 N mm^{-1} , and the dissipated energy (the enclosed area) rises by 17-folds from 52.69 to 892.73 mJ . Figure 3g indicates that the artificial IVD can dissipate more energy when the patient engages in more intensive activity. Furthermore, we performed cyclic loading tests on the artificial IVD to explore the effects of compressive pre-strain (ε_{pre}) and loading frequency on its energy dissipation capability, which is quantified by loss factor ($\tan\delta$). Details on experiments and analyses can be seen in Text S15 and Figure S17 (Supporting Information). Note that the loading frequency range (0.1 – 5 Hz) can effectively capture the daily operational frequencies of IVDs.^[50,51] As shown in Figure 3h, under the same loading frequency, the increase in ε_{pre} (body weight) leads to the rise in $\tan\delta$. The $\tan\delta$ is higher (over 1.5 and even ≈ 2) when the loading frequency increases to 5 Hz .

As illustrated in Figure 3i, we conducted cyclic torsion tests on the C2T artificial IVD to evaluate its capability of dissipating the energy that might be generated from waist twisting. Details on the experiments can be seen in the Experimental Section. Figure 3j presents the typical hysteresis loop (Lissajous curve), which can reflect the energy dissipation characteristics of the C2T artificial IVD under dynamic torsion. The dissipated energy is the area of the hysteresis loop, which can be calculated as $\pi\gamma^2 E''$ where γ is the amplitude of shear strain. Detailed derivations can be seen in Text S16 (Supporting Information). When the oscillation frequency increases from 0.1 to 5 Hz , the dissipated strain energy density rises from 0.56 and 3.09 J cm^{-3} , which can be at-

tributed to the positive correlation between loss modulus E'' of the HED polymer and frequency f (Figure 1i). Moreover, we can use the cyclic torsion tests to investigate the effects of compressive pre-strain (ε_{pre}) and loading frequency (f) on the energy dissipation capability ($\tan\delta$) of artificial IVD. As shown in Figure 3k, under the same loading frequency, higher ε_{pre} leads to higher $\tan\delta$; under the same ε_{pre} , $\tan\delta$ increases with the rise in loading frequency. Furthermore, fatigue tests performed on both the HED polymer and the 3D C2T structure confirm their structural integrity and stable energy dissipation performance under long-term cyclic loading, demonstrating suitability for sustained operational use (Text S17 and Figure S19, Supporting Information).

2.4. Low-Frequency and Bandgap Tunable Vibration Isolation Meta-Device Enabled by 3D C2T Structure

Low-frequency vibrations (<250 Hz)^[52] pose significant challenges in precision instrumentation and human comfort due to their long-wavelength penetration characteristics. Vibration isolators are the materials or structures used to dissipate or isolate the low-frequency vibrations. Conventional non-viscoelastic isolators achieve isolation of low-frequency vibrations through spring-damper metadevices, which are relatively complex and costly. An alternative is viscoelastic isolators, which operate by transmitting external vibrations to the viscoelastic material through compression or shear; the material then dissipates energy via internal mechanisms (e.g., polymer chain movement), enabling isolation within a specific band. However, the performance of these viscoelastic isolators is limited: their frequency-dependent damping declines sharply beyond certain cut-off frequencies,^[53,54] narrowing the effective isolation bandgap. Moreover, most existing viscoelastic isolators employ a bulk material design, which limits their stiffness adjustment range and makes it difficult to achieve broadband low-frequency vibration isolation.^[27,43]

To overcome these limitations, we leverage the compression-to-tension (C2T) design, which effectively decouples the material's intrinsic dissipation properties from the structural stiffness. This design enables direct tuning of the bandgap by adjusting the C2T's structural stiffness. Additionally, the HED component's high loss factor and high strain-rate sensitivity (outperforming conventional materials) are key to achieving a broader isolation bandwidth. Here, we employ the C2T structure to develop low-frequency vibration isolators (VIs) and VI metadevices where we can freely tune the location and width of the frequency isolation bandgap by varying the design and deployment of the C2T structures. Figure 4a illustrates the proposed VI, which includes the C2T structure placed between the rigid frame and counterweight. To evaluate the performance of the proposed VI, we built a dynamic testing apparatus (Figure 4b; Figure S20, Supporting Information) which mainly includes a shaker to generate low-frequency vibration, an accelerometer placed on the shaker to measure the input excitation force $F_{\text{in}}(\omega)$, and an accelerometer attached on the top of the rigid frame to measure the output filtered force $F_{\text{out}}(\omega)$. Performance of a VI is characterized by the dynamic transmission characteristic $T(\omega)$, which can be calculated as $T(\omega) = F_{\text{out}}(\omega)/F_{\text{in}}(\omega)$. Figure 4c presents the performance characterization of the C2T structure-based VI, where a broad

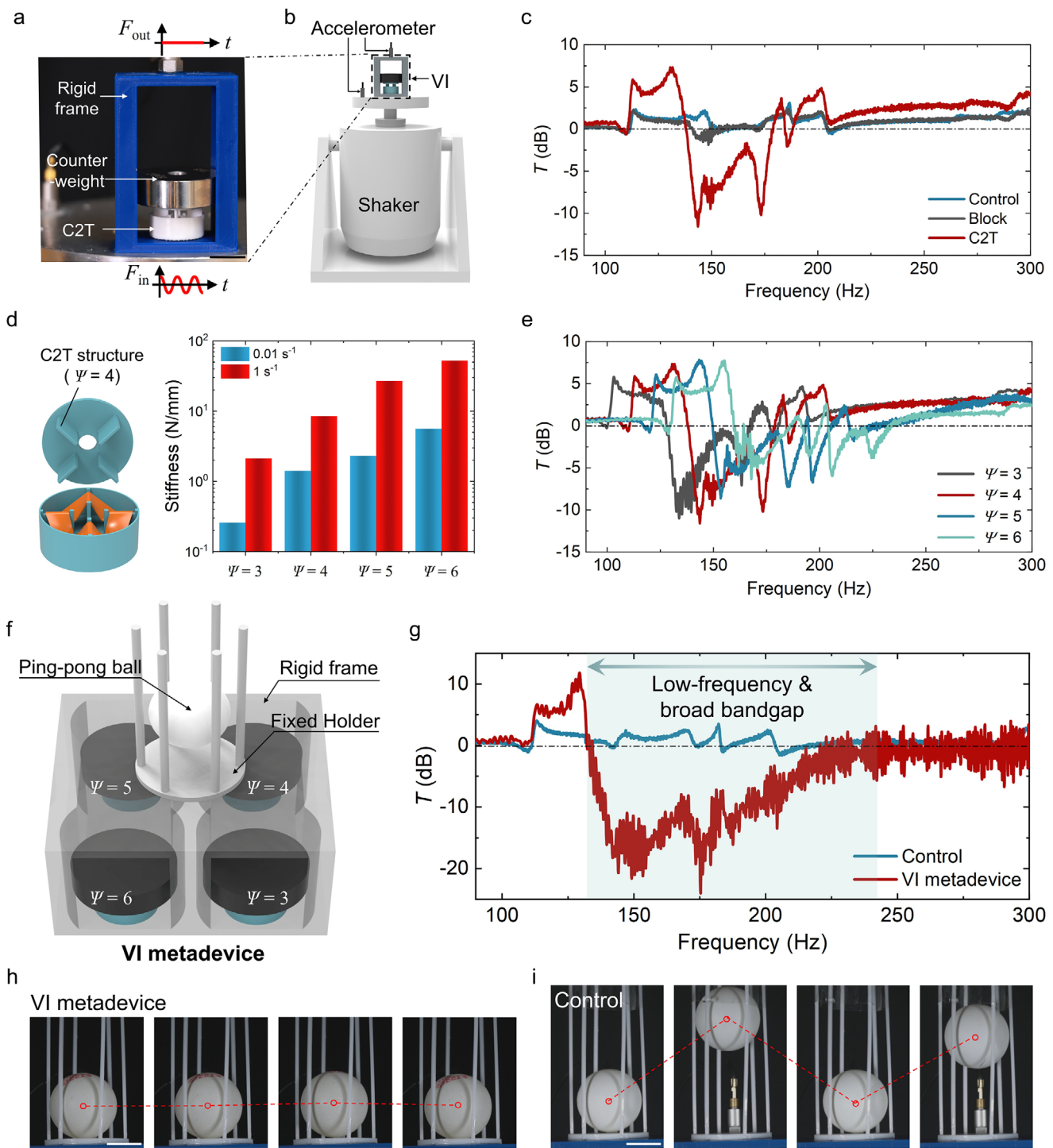


Figure 4. C2T structure-based VI metadevice for low-frequency vibration isolation with wide bandgap tunability. **a)** Snapshot of the C2T structure-based VI comprising a C2T structure, counterweight, and rigid frame. **b)** Schematic diagram presenting the dynamic vibration testing setup. **c)** Vibration isolation performances of the C2T structure-based VI, and the other two comparing structures. **d)** Compression tests under different loading rates showing that the stiffness and damping effect are enhanced by increasing the section number ($\Psi = 3\text{--}6$). **e)** Vibration isolation performance of VIs with different Ψ values. **f)** Schematic illustration of the VI metadevice consisting of four VIs with different Ψ values. **g)** Vibration isolation performance presenting the superior broadband low-frequency vibration isolation performance of the VI metadevice. **h,i)** Ping-pong ball demonstrations showing that the VI metadevice (**h**) is capable of isolating the low-frequency vibration from 150 Hz to 250 Hz, while the control structure (**i**) fails to do so. Scale bar: 20 mm.

vibration isolation bandgap (the frequency range where $T(\omega)$ is less than zero) spans from 137.4 to 179.1 Hz, achieving a maximum attenuation of -12 dB. In comparison, we also tested the vibration isolation performance of two comparison structures: the one with only a rigid frame (control), and the other one where HED bulk material replaces the HED C2T structure. However, no apparent vibration isolation band gaps are found on the performance characterizations of the two compared structures.

To elucidate the vibration isolation mechanism of the C2T structure-based VI (Text S18, Supporting Information), we develop a theoretical model that calculates $T(\omega)$ in terms of the rigid frame mass M and the effective mass $m_{\text{eff}}(\omega)$ of the C2T structure-based VI:

$$T(\omega) = \frac{M}{m_{\text{eff}}(\omega)} \quad (2)$$

where $m_{\text{eff}}(\omega)$ is correlated with stiffness k and damping coefficient $c(\omega)$ of the C2T structure:

$$m_{\text{eff}}(\omega) = M + m \frac{k - i \cdot c(\omega) \omega}{k - \omega^2 m - i \cdot c(\omega) \omega} \quad (3)$$

The theoretical model predictions (Figures S21, Supporting Information) show that an increase in k shifts the resonance frequency (the frequency range where $T(\omega)$ is much greater than one) to higher values, and an increase in $c(\omega)$ broadens the isolation bandgap. In fact, we can tune k and $c(\omega)$ of the HED C2T structure by varying the section number Ψ . As shown in Figure 4d and Figure S22 (Supporting Information), under compression of slow strain rate (0.01 s $^{-1}$), where the effect of damping can be ignored, an increase in Ψ (from 3 to 6) leads to the rise of structure stiffness (from 0.18 to 4.5 N mm $^{-1}$). Under high strain rate (1 s $^{-1}$) where the damping effect dominates, the stiffness of the C2T structure increases from 2.16 to 38.54 N mm $^{-1}$ as Ψ increases from 3 to 6. Figure 4e presents that the increase in Ψ moves the resonance frequency toward higher values, and broadens the isolation bandgap, which agrees well with the trend predicted by the theoretical model.

To further broaden the vibration isolation bandgap, as illustrated in Figure 4f, we develop a VI metadevice consisting of four VIs with Ψ ranging from 3 to 6. The vibration testing result (Figure 4g) shows that the VI metadevice attained a maximum attenuation of -20 dB across 130 – 240 Hz (≈ 110 Hz bandwidth)—a threefold increase in bandwidth compared to a single VI unit, highlighting its superior broadband low-frequency vibration isolation performance. In comparison, the result of the vibration test on the control structure, which only has four rigid frames, exhibits no distinct isolation bandgap across the testing frequency spectrum. To visually demonstrate the outstanding vibration isolation capability of the VI metadevice, we applied broadband low-frequency vibration excitations ranging from 150 to 250 Hz to it, where a Ping-pong ball is placed. As shown in Figure 4h, the VI metadevice can successfully isolate the low-frequency vibration so that the Ping-pong ball remained stationary while the vibration with varying frequencies was applied (Movie S2, Supporting Information). In contrast, the Ping-pong ball on the control structure was constantly bouncing (Figure 4i) when the same vibration was applied.

3. Conclusion

In this work, we develop the high-energy-dissipating (HED) polymers, which can synchronously achieve high loss factor ($\tan\delta$ up to 2), high modulus (up to 110.5 MPa), high stretchability (up to 1470.7%), and high dissipated energy density (up to 26.8 J cm $^{-3}$). We attribute such extraordinary energy dissipation capability of the HED polymers to two types of dynamic physical crosslinks (hydrogen bonds and dynamic coordination bonds). We conduct experiments and theoretical modeling to validate the above hypothesis. We design HED-based compression-to-tension (C2T) structures that convert compression on them to tension on the HED strips to fully liberate tension-induced high energy dissipation of the HED polymers. Then, we use DLP-based multimaterial 3D printing for fabricating the C2T structures whose energy dissipation capability is adaptive by tuning the geometric parameters, and ≈ 100 times higher than that of octet structures made of pure HED polymer. To demonstrate the adaptive capability of dissipating impact and vibration energies, we employ the C2T structures to form artificial IVDs and low-frequency vibration isolators. Despite these advancements, we acknowledge that certain limitations—such as extreme scalability (across micro and macro scales), performance under broader environmental and loading conditions (e.g., very high strain rates, varying humidity/temperature), and comprehensive biocompatibility testing for biomedical applications—remain to be fully explored, providing fruitful avenues for future research. These challenges outline a promising roadmap, where future efforts will focus on geometric optimization of the C2T architecture to enhance strain range and mitigate anisotropy, expansion of testing regimes to quantify real-world impact and vibration scenarios, integration of advanced multi-material manufacturing techniques to overcome scalability constraints, and dedicated investigations into long-term stability, degradation, and biocompatibility for biomedical translations. Addressing these aspects will not only overcome current limitations but also significantly broaden the application horizon of these adaptive energy-dissipating metadevices in fields such as electronics, bio-implants, and precision instruments.

4. Experimental Section

Materials: Acrylic acid (AAc), N-(2-Hydroxyethyl) acrylamide (HEAA), 4-hydroxybutylacrylate (HBA), zinc acrylate (ZA), and 2,4,6-trimethylbenzoyl diphenylphosphine oxide (TPO) were purchased from Sigma-Aldrich (Shanghai) and used as received. VHB (Very High Bond) material was obtained by cutting 3M VHB tape, which was purchased from 3 M Corp., and used as received. PDMS (Polydimethylsiloxane) material was purchased from Hangzhou Westru Technology Co, Ltd. and used as received.

Precursor Solution Preparation: The HED precursor was prepared by mixing 12.5 wt.% acrylic acid (AAc), 12.5 wt.% N-(2-Hydroxyethyl) acrylamide (HEAA), and 75 wt.% 4-hydroxybutylacrylate (HBA), as well as 0.75 wt.% zinc acrylate (ZA) of the total weight of monomers. In addition, 2 wt.% 2,4,6-trimethylbenzoyl diphenylphosphine oxide (TPO) of the total weight of monomers was added as the photoinitiator. The HED without the ZA precursor was prepared by mixing 12.5 wt.% AAc, 12.5 wt.% HEAA, and 75 wt.% HBA. In addition, 2 wt.% TPO of the total weight of monomers was added as the photoinitiator.

Gel Permeation Chromatography Tests: The molecular weights of HED and HED without ZA were measured using an Agilent-1260 metadevice (Agilent Technologies, USA). Samples were dissolved in

- [20] K. Liu, L. Cheng, N. Zhang, H. Pan, X. Fan, G. Li, Z. Zhang, D. Zhao, J. Zhao, X. Yang, *J. Am. Chem. Soc.* **2020**, *143*, 1162.
- [21] J. Huang, Y. Xu, S. Qi, J. Zhou, W. Shi, T. Zhao, M. Liu, *Nat. Commun.* **2021**, *12*, 3610.
- [22] G. Chen, J. Wu, Z. Wang, H. Zhu, S. Zhu, Q. Zhang, *Sci. Adv.* **2025**, *11*, adv5292.
- [23] Y. Wu, Y. Wang, X. Guan, H. Zhang, R. Guo, C. Cui, D. Wu, Y. Cheng, Z. Ge, Y. Zheng, *Adv. Mater.* **2023**, *35*, 2306882.
- [24] C. Zhao, X. Gong, S. Wang, W. Jiang, S. Xuan, *Cell Reports Physical Science* **2020**, *1*, 100266.
- [25] M. Wei, K. Lin, L. Sun, *Materials and Design* **2022**, *216*, 110570.
- [26] C. Zhao, Y. Wang, M. Ni, X. He, S. Xuan, X. Gong, *Composites, Part A* **2021**, *143*, 106285.
- [27] M. O. Saed, W. Elmadih, A. Terentjev, D. Chronopoulos, D. Williamson, E. M. Terentjev, *Nat. Commun.* **2021**, *12*, 6676.
- [28] D. Mistry, N. A. Traugutt, B. Sanborn, R. H. Volpe, L. Chatham, R. Zhou, B. Song, K. Yu, K. Long, C. M. Yakacki, *Nat. Commun.* **2021**, *12*, 6677.
- [29] Z. Yang, Y. Yang, H. Liang, E. He, H. Xu, Y. Liu, Y. Wang, Y. Wei, Y. Ji, *Nat. Commun.* **2024**, *15*, 9902.
- [30] M. Dong, Y. Han, X. P. Hao, H. C. Yu, J. Yin, M. Du, Q. Zheng, Z. L. Wu, *Adv. Mater.* **2022**, *34*, 2204333.
- [31] N. A. Traugutt, D. Mistry, C. Luo, K. Yu, Q. Ge, C. M. Yakacki, *Adv. Mater.* **2020**, *32*, 2000797.
- [32] W. Z. Jiang, X. C. Teng, X. H. Ni, X. G. Zhang, X. Cheng, W. Jiang, D. Han, Y. Zhang, X. Ren, *Engineering Structures* **2024**, *307*, 117318.
- [33] Y. Zhang, W. Z. Jiang, W. Jiang, X. Y. Zhang, J. Dong, Y. M. Xie, K. E. Evans, X. Ren, *Adv. Funct. Mater.* **2025**, 2421746.
- [34] V. Deshpande, M. Ashby, N. Fleck, *Acta Mater.* **2001**, *49*, 1035.
- [35] M. A. Wagner, T. S. Lumpe, T. Chen, K. Shea, *Extreme Mechanics Letters* **2019**, *29*, 100461.
- [36] B. Deng, R. Xu, K. Zhao, Y. Lu, S. Ganguli, G. J. Cheng, *Mater. Today* **2018**, *21*, 467.
- [37] Q. Liu, H. Ye, J. Cheng, H. Li, X. He, B. Jian, Q. Ge, *Acta Mechanica Solida Sinica* **2023**, *36*, 582.
- [38] D. C. Kong, M. H. Yang, X. S. Zhang, Z. C. Du, Q. Fu, X. Q. Gao, J. W. Gong, *Macromol. Mater. Eng.* **2021**, *306*, 2100536.
- [39] A. P. Dhand, M. D. Davidson, H. M. Zlotnick, T. J. Kolibaba, J. P. Killgore, J. A. Burdick, *Science* **2024**, *385*, 566.
- [40] A. Jangizehi, M. Ahmadi, S. Seiffert, *Mater. Adv.* **2021**, *2*, 1425.
- [41] A. P. Unwin, P. J. Hine, I. M. Ward, M. Fujita, E. Tanaka, A. A. Gusev, *Sci. Rep.* **2018**, *8*, 2454.
- [42] B. Park, J. H. Shin, J. Ok, S. Park, W. Jung, C. Jeong, S. Choy, Y. J. Jo, T.-i. Kim, *Science* **2022**, *376*, 624.
- [43] Y. Hou, Y. Peng, P. Li, Q. Wu, J. Zhang, W. Li, G. Zhou, J. Wu, *ACS Applied Materials and Interfaces* **2022**, *14*, 35097.
- [44] M. Humzah, R. Soames, *The Anatomical Record* **1988**, *220*, 337.
- [45] D. Hoy, L. March, P. Brooks, F. Blyth, A. Woolf, C. Bain, G. Williams, E. Smith, T. Vos, J. Barendregt, *Ann. Rheum. Dis.* **2014**, *73*, 968.
- [46] A. Freemont, *Rheumatology* **2009**, *48*, 5.
- [47] M. D. Helgeson, A. J. Belevino, A. S. Hilibrand, *The spine journal* **2013**, *13*, 342.
- [48] Y. Jiang, K. Shi, L. Zhou, M. He, C. Zhu, J. Wang, J. Li, Y. Li, L. Liu, D. Sun, *Bioactive materials* **2023**, *20*, 528.
- [49] W. Fan, Z. Qian, G. Song, K. Wang, F. Galbusera, L. Ren, H. J. Wilke, L. Ren, *Adv. Funct. Mater.* **2025**, *35*, 2414275.
- [50] J. J. Costi, I. A. Stokes, M. G. Gardner-Morse, J. C. Iatridis, *Spine* **2008**, *33*, 1731.
- [51] D. Lazaro-Pacheco, I. Ebisch, T. Holsgrove, *J. Biomech.* **2024**, *163*, 111919.
- [52] J. Kantor, Z. Vilímek, M. Vítězník, P. Smrčka, E. A. Campbell, M. Bucharová, J. Grohmannová, G. Špinarová, K. Janíčková, J. Du, *Frontiers in psychology* **2022**, *13*, 980756.
- [53] A. Sakhnevych, R. Maglione, R. Suero, L. Mallozzi, *Nonlinear Dyn.* **2024**, *112*, 21729.
- [54] X. Zhou, D. Yu, X. Shao, S. Zhang, S. Wang, *Compos. Struct.* **2016**, *136*, 460.
- [55] J. Cheng, R. Wang, Z. Sun, Q. Liu, X. He, H. Li, H. Ye, X. Yang, X. Wei, Z. Li, *Nat. Commun.* **2022**, *13*, 7931.